CAMSAP3 facilitates basal body polarity and the formation of the central pair of microtubules in motile cilia

Alan M. Robinson[a], Satoe Takahashi[a], Eva J. Brotslaw[b], Aisha Ahmad[c], Emma Ferrer[a], Daniele Procissi[d], Claus-Peter Richter[a,c,e], Mary Ann Cheatham[c,e], Brian J. Mitchell[b], and Jing Zheng[a,c,e,1]

[a]Department of Otolaryngology–Head and Neck Surgery, Northwestern University, Chicago, IL 60611; [b]Department of Cell and Developmental Biology, Northwestern University, Chicago, IL 60611; [c]Department of Communication Sciences and Disorders, Northwestern University, Evanston, IL 60208; [d]Department of Radiology, Feinberg School of Medicine, Northwestern University, Chicago, IL 60611; and [e]Knowles Hearing Center, Northwestern University, Evanston, IL 60208

Edited by Hannah Mitchison, University College London, London, United Kingdom, and accepted by Editorial Board Member Kathryn V. Anderson April 16, 2020 (received for review April 29, 2019)

Synchronized beating of cilia on multiciliated cells (MCCs) generates a directional flow of mucus across epithelia. This motility requires a "9 + 2" microtubule (MT) configuration in axonemes and the unidirectional array of basal bodies of cilia on the MCCs. However, it is not fully understood what components are needed for central MT-pair assembly as they are not continuous with basal bodies in contrast to the nine outer MT doublets. In this study, we discovered that a homozygous knockdown mouse model for MT minus-end regulator calmodulin-regulated spectrin-associated protein 3 (CAMSAP3), *Camsap3*$^{tm1a/tm1a}$, exhibited multiple phenotypes, some of which are typical of primary ciliary dyskinesia (PCD), a condition caused by motile cilia defects. Anatomical examination of *Camsap3*$^{tm1a/tm1a}$ mice revealed severe nasal airway blockage and abnormal ciliary morphologies in nasal MCCs. MCCs from different tissues exhibited defective synchronized beating and ineffective generation of directional flow likely underlying the PCD-like phenotypes. In normal mice, CAMSAP3 localized to the base of axonemes and at the basal bodies in MCCs. However, in *Camsap3*$^{tm1a/tm1a}$, MCCs lacked CAMSAP3 at the ciliary base. Importantly, the central MT pairs were missing in the majority of cilia, and the polarity of the basal bodies was disorganized. These phenotypes were further confirmed in MCCs of *Xenopus* embryos when CAMSAP3 expression was knocked down by morpholino injection. Taken together, we identified CAMSAP3 as being important for the formation of central MT pairs, proper orientation of basal bodies, and synchronized beating of motile cilia.

CAMSAP3 | motile cilia | primary ciliary dyskinesia | central MT pair | basal body orientation

Microtubules (MTs) are dynamic, polymeric polar tubes: The fast-growing plus end leads to MT elongation, while the slow-growing minus end attaches to various cellular structures such as basal bodies. CAMSAP3 (calmodulin-regulated spectrin-associated protein 3), also called Marshalin (1), is an MT minus-end regulator that stabilizes MTs (2, 3). CAMSAP3 has multiple protein–protein interaction domains (*SI Appendix*, Fig. S1*A*) that permit interactions with other partners to regulate MT networks, organelle positioning, and MT polarity (1–7). In addition, CAMSAP3 is involved in the formation of MTs from a noncentrosomal MT-organizing center (ncMTOC) as CAMSAP3-coated MTs are stable and capable of acting as seeds for MT elongation (8, 9). For example, CAMSAP3 is involved in forming ncMTOCs in preimplantation embryos when the centrosome, a prevalent MTOC, is not present (10). Because CAMSAP3 is widely expressed, knockout or reducing *Camsap3* expression was reported to have multiple defects in placenta (11), neurons (8, 12), and enterocytes of the gastrointestinal tract (13, 14). Unexpectedly, we discovered that CAMSAP3 is also expressed in multiciliated cells (MCCs).

MCCs are restricted to luminal surfaces as in the nasal cavity, trachea, middle ear, Eustachian tube, reproductive tract, and ventricles of the brain (15). Each MCC displays hundreds of motile cilia protruding from basal bodies under the apical membrane. A complicated transcriptome and multitier pathways are devoted to MT-based multiciliogenesis (16–19). Mature motile cilia are thought to consist of over 600 proteins, whose identities and functions are far from being completely understood. Because cilia are highly conserved structures, dysfunction of motile cilia impacts a diverse set of tissues and causes primary ciliary dyskinesia (PCD). This complex disorder can include embryonic lethality, infertility, hydrocephalus, and dysfunctional mucus clearance, which leads to anosmia or hyposmia, sinusitis, respiratory distress, otitis media, and hearing loss (15). A key step in understanding the mechanism(s) underlying PCD is to identify the components that participate in the generation of motile cilia, so that their functions can be characterized in vivo. Due to the importance of cilia in developmental signaling, mutations that affect all cilia are often embryonically lethal, making detailed analysis challenging.

Significance

Cilia are composed of hundreds of proteins whose identities and functions are far from being completely understood. In this study, we determined that calmodulin-regulated spectrin-associated protein 3 (CAMSAP3) plays an important role for the function of motile cilia in multiciliated cells (MCCs). Global knockdown of CAMSAP3 protein expression in mice resulted in defects in ciliary structures, polarity, and synchronized beating in MCCs. These animals also displayed signs and symptoms reminiscent of primary ciliary dyskinesia (PCD), including a mild form of hydrocephalus, subfertility, and impaired mucociliary clearance that leads to hyposmia, anosmia, rhinosinusitis, and otitis media. Functional characterization of CAMSAP3 enriches our understanding of the molecular mechanisms underlying the generation and function of motile cilia in MCCs.

Author contributions: A.M.R., S.T., M.A.C., B.J.M., and J.Z. designed research; A.M.R., S.T., E.J.B., A.A., E.F., D.P., C.-P.R., and J.Z. performed research; A.M.R., S.T., E.J.B., D.P., C.-P.R., B.J.M., and J.Z. analyzed data; A.M.R., S.T., C.-P.R., M.A.C., B.J.M., and J.Z. wrote the manuscript with input from all authors.

The authors declare no competing interest.

This article is a PNAS Direct Submission. H.M. is a guest editor invited by the Editorial Board.

[1]To whom correspondence may be addressed. Email: jzh215@northwestern.edu.

This article contains supporting information online at https://www.pnas.org/lookup/suppl/doi:10.1073/pnas.1907335117/-/DCSupplemental.

First published June 1, 2020.

To produce a directional fluid flow that transports materials across the epithelium, hundreds of cilia on MCCs need to move in a synchronized manner. A unidirectional array of basal bodies in MCCs is required to achieve synchronized beating (16, 20, 21). This polarized array is achieved by a combination of planar cell polarity (PCP) signaling, cytoskeletal dynamics, and hydrodynamic forces (22). Unlike most primary cilia, which lack a central pair, motile cilia maintain a "9 + 2" MT configuration in their axonemes with two MT singlets surrounded by nine MT doublets (18). The central MTs and their associated proteins form the central apparatus (23), which is essential for planar motion rather than rotational beating (24). Unlike the outer nine MT doublets, the central MT pair is not continuous with MT triplets in the basal body (25). How the central MT pair is assembled, and what components are required, is still not fully understood.

In this study, we investigated a knockdown (KD) mouse model, *Camsap3*^{tm1a}, that we rederived on CBA/CaJ and FVB murine strain backgrounds. Homozygous *Camsap3*$^{tm1a/tm1a}$ mice exhibited multiple pathological phenotypes. Many of these phenotypes are similar to those of PCD, including subfertility in both sexes and severe nasal airway blockage leading to coughing, sneezing, hyposmia, and rhinosinusitis. Since PCD is a condition caused by motile cilia defects and CAMSAP3-coated MTs are known to be involved in many cellular functions (4–10), we suspected that CAMSAP3 plays an important role(s) for motile cilia function. To test this possibility, we investigated the function of MCCs in different tissues. Our data show that CAMSAP3 localizes to the base of axonemes and at the basal bodies in normal MCCs. In contrast, the majority of cilia in *Camsap3*$^{tm1a/tm1a}$ lack the central MT pair in their axoneme and display disorientated basal bodies and defects in ciliary motion, which is no longer synchronized. The latter phenotype likely underlies their PCD-like behaviors. Since multiciliogenesis is remarkably well conserved throughout eukaryotes (26), we further investigated CAMSAP3's function in MCCs in early *Xenopus* embryos. *Xenopus* embryos injected with *Camsap3* morpholinos to knock down expression also exhibited defective ciliary function and abnormal morphology. Taken together, our data suggest that CAMSAP3 is required for normal motile cilia function.

Results

Strain-Dependent Subviability of the CAMSAP3-KD Mouse Model *Camsap3*^{tm1a}. Originally, a *Camsap3*^{tm1a} mouse model on the C57BL6N background was created using the "knockout first, conditional-ready" strategy (27). A targeted trap allele was inserted into the intron between exons 6 and 7 of the *Camsap3* gene to knock out *Camsap3* expression through RNA processing (28, 29) without deleting any exons (Fig. 1*A*). However, *Camsap3*$^{tm1a/tm1a}$ showed preweaning mortality and very low reproductive rates. Among 104 mice, *Camsap3*^{tm1a} breeders on the C57B6N background had only two *Camsap3*$^{tm1a/tm1a}$ pups (*SI Appendix*, Table S1). This observation was consistent with the available data on Deciphering the Mechanisms of Developmental Disorders (DMDD; https://dmdd.org.uk/), which indicated that *Camsap3*$^{tm1a/tm1a}$ were subviable. In addition, we did not observe obvious behavioral or gross structural differences between wild-type (WT) and *Camsap3*$^{tm1a/+}$ mice. In order to obtain more *Camsap3*$^{tm1a/tm1a}$, we rederived this line on CBA/CaJ and FVB murine backgrounds. *Camsap3*^{tm1a} mice on the FVB background overcame the severe subviability issue in the original background and were born at Mendelian ratios: 1:2:1 for WT, heterozygote (*Camsap3*$^{tm1a/+}$), and homozygote (*Camsap3*$^{tm1a/tm1a}$) (*SI Appendix*, Table S1).

We confirmed that *Camsap3* transcripts were indeed decreased in *Camsap3*$^{tm1a/tm1a}$ in both FVB and CBA/CaJ backgrounds (*SI Appendix*, Fig. S2 *A–C*) but not completely absent as reported in other *tm1a* alleles using the same strategy (29). To test whether CAMSAP3 proteins were present in *Camsap3*$^{tm1a/tm1a}$, brain lysates from male and female littermates were analyzed using anti–CAMSAP3-M, whose antigen specificity was verified by both immunofluorescence (IF) and Western blot analyses (*SI Appendix*, Fig. S1). Although the degree of CAMSAP3 reduction varied among individuals from the same litter (Fig. 1*B* and *SI Appendix*, Fig. S2 *D–F*), the reduction in CAMSAP3 protein expression was statistically significant in *Camsap3*$^{tm1a/tm1a}$. Hence, the *Camsap3*^{tm1a} mouse model is hypomorphic for CAMSAP3 but not a null.

We observed domed heads, a mild form of hydrocephalus, in some postnatal *Camsap3*$^{tm1a/tm1a}$ mice on the CBA/CaJ background (*SI Appendix*, Fig. S3*A*) but seldom observed this change in animals on the FVB background. However, snout asymmetry in *Camsap3*$^{tm1a/tm1a}$ was observed for both CBA/CaJ and FVB strain backgrounds (*SI Appendix*, Fig. S3*B*), although the penetrance was incomplete. Heterozygotes of all strains were indistinguishable from WT. These data reinforce the notion that genetic background impacts the severity of phenotypes observed in *Camsap3*$^{tm1a/tm1a}$ mice.

Characterization of *Camsap3*^{tm1a} Mice. We examined *Camsap3*^{tm1a} at three stages: neonatal (postnatal day [P] ~3), adolescent/young adult (3 wk to 3 mo), and older mice (>6 mo). *Camsap3*$^{tm1a/tm1a}$ consistently exhibited some of the phenotypes that are often associated with PCD regardless of sex and strain backgrounds. Heterozygotes were indistinguishable from wild type.

1) Low body weight. *Camsap3*$^{tm1a/tm1a}$ were born smaller than their WT and *Camsap3*$^{tm1a/+}$ littermates, and remained smaller into adulthood. The mean weights at P3 to 4 in g ± SD were as follows: WT and *Camsap3*$^{tm1a/+}$, 2.7 ± 0.5; *Camsap3*$^{tm1a/tm1a}$, 1.7 ± 0.4 (Fig. 1*C*); at P184 to 248, WT and *Camsap3*$^{tm1a/+}$, 42.23 ± 7.077; *Camsap3*$^{tm1a/tm1a}$, 23.7 ± 2.862 (Fig. 1*D*). Unpaired *t* test with Welch's correction revealed statistically significant reduction in *Camsap3*$^{tm1a/tm1a}$ for both age groups.
2) Subfertility in both sexes. Compared with WT, average fertility was significantly reduced for male *Camsap3*$^{tm1a/tm1a}$ and even further reduced for female *Camsap3*$^{tm1a/tm1a}$ (Fig. 1*E*). Mean ± SD are as follows: WT x WT, 90.63 ± 11.97; male *Camsap3*$^{tm1a/tm1a}$ x female WT, 43.13 ± 23.31; female *Camsap3*$^{tm1a/tm1a}$ x male WT, 14.40 ± 17.56. One-way ANOVA with Dunnett's multiple-comparison test showed that both male and female *Camsap3*$^{tm1a/tm1a}$ had significantly lower fertility (*P* values are as indicated). Furthermore, average litter sizes (Fig. 1*F*) were similar between WT and *Camsap3*$^{tm1a/tm1a}$ males but significantly decreased for female *Camsap3*$^{tm1a/tm1a}$ compared with WT x WT. Mean litter sizes ± SD are as follows: WT x WT, 9.0 ± 2.9; male *Camsap3*$^{tm1a/tm1a}$ x female WT, 9.8 ± 3.1; male WT x female *Camsap3*$^{tm1a/tm1a}$, 2.2 ± 0.4. One-way ANOVA with Dunnett's multiple-comparison test revealed that male *Camsap3*$^{tm1a/tm1a}$ do not have significant differences, while female *Camsap3*$^{tm1a/tm1a}$ had significantly fewer pups per litter.
3) Coughing and sneezing. *Camsap3*$^{tm1a/tm1a}$ produced audible "wheezing" in both sexes (Movie S1). The amplitudes of the soundtracks in *Camsap3*$^{tm1a/tm1a}$ were larger than for their age-matched WT (*SI Appendix*, Fig. S4). Sneezing was also audible in *Camsap3*$^{tm1a/tm1a}$ mice (Audio S1).
4) Olfactory dysfunction. Mice were placed in a cage with hidden food to test olfactory function (buried food assay). Young adult mice were able to find the hidden food regardless of their genotype, suggesting that they had functional olfaction (WT, $n = 7$; *Camsap3*$^{tm1a/+}$, $n = 9$; *Camsap3*$^{tm1a/tm1a}$, $n = 16$). In contrast, when older mice were tested, none of the *Camsap3*$^{tm1a/tm1a}$ could find food, while all control mice (WT and *Camsap3*$^{tm1a/+}$) did (Fig. 1*G*), suggesting *Camsap3*$^{tm1a/tm1a}$ progressively lost their sense of smell. One-way ANOVA was

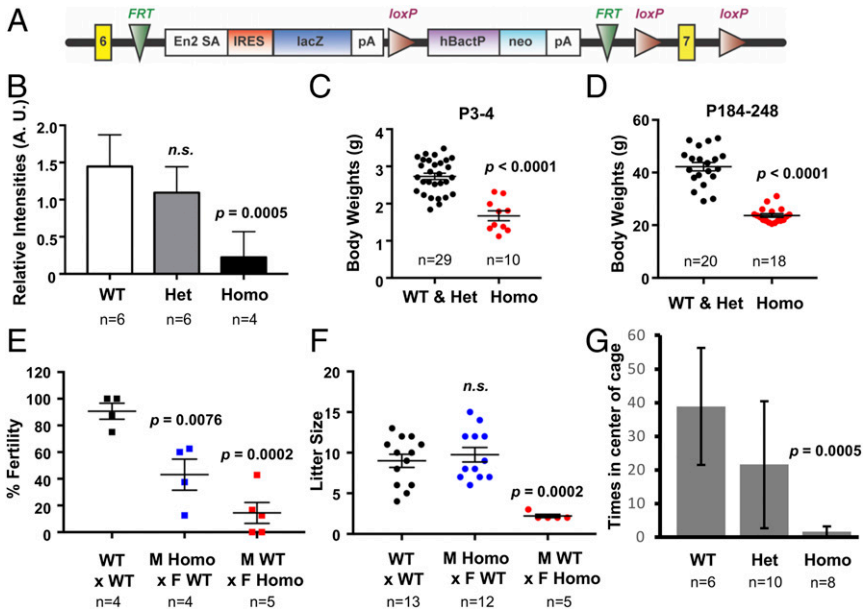

Fig. 1. Phenotypes of the *Camsap3*^{tm1a} mouse model. (*A*) Structure of the *Camsap3*^{tm1a} allele with an RNA-processing signal/lacZ-trapping element inserted between exons 6 and 7 (indicated as yellow boxes) of the *Camsap3* gene. (*B*) CAMSAP3 expression is significantly decreased in *Camsap3*$^{tm1a/tm1a}$. Relative intensities in arbitrary units of CAMSAP3 bands from three independent Western blots using brain lysates from P10 to 11 littermates. Intensities are normalized to tubulin-loading control bands (detected by anti–α-tubulin). (*C* and *D*) Body weight is significantly decreased in *Camsap3*$^{tm1a/tm1a}$. Weight of neonatal mice ages P3 to 4 (*C*) and older adult mice ages P184 to 248 (*D*) versus genotype. (*E* and *F*) Fertility and litter size are significantly decreased in *Camsap3*$^{tm1a/tm1a}$. Fertility rate (*E*) and mean litter sizes (*F*) for breeding pairs of the indicated genotypes. M, male; F, female. (*G*) Food finding is significantly decreased in older adult *Camsap3*$^{tm1a/tm1a}$. Mean number of times mice were found in the center of a cage with hidden food versus genotype. Het, *Camsap3*$^{tm1a/+}$; Homo, *Camsap3*$^{tm1a/tm1a}$. *n*, number of animals; n.s., not statistically significant. Error bars are standard deviations from the means.

performed to compare the mean number of times mice were found in the center of a cage with hidden food. The Tukey–Kramer test indicated that WT mice were not significantly different from *Camsap3*$^{tm1a/+}$, but both WT and *Camsap3*$^{tm1a/+}$ were significantly different from *Camsap3*$^{tm1a/tm1a}$ ($P = 0.0005$).

5) Mucin accumulation and rhinosinusitis. Animals at different ages showed mucin accumulation to various degrees ($n = 10$). For older mice, all *Camsap3*$^{tm1a/tm1a}$ had accumulated mucin that almost completely obstructed the nasal passage, as detected by periodic acid Schiff (PAS) staining (Fig. 2*B*). The nasal septum was noticeably deviated (arrows in Fig. 2*B*) and the turbinates were displaced in *Camsap3*$^{tm1a/tm1a}$ as compared with WT (Fig. 2*A*). Mucin accumulation was also found around the ethmoid turbinates that are enriched in the olfactory epithelium (Fig. 2*D*) and maxillary sinus (*SI Appendix*, Fig. S5). Accumulated mucin also extended to the Eustachian tube, even in young adult *Camsap3*$^{tm1a/tm1a}$ mice (Fig. 2*F*), but not in WT (Fig. 2 *C* and *E*). For young adult mice, microcomputed tomography (micro-CT) and MRI were performed to reveal nasal blockage and structural abnormalities (WT, $n = 1$; *Camsap3*$^{tm1a/+}$, $n = 2$; *Camsap3*$^{tm1a/tm1a}$, $n = 3$). MRI images show the airway blockage in *Camsap3*$^{tm1a/tm1a}$ but not in WT (Fig. 2 *G* and *H* and *SI Appendix*, Fig. S6). Three-dimensional (3D) rendered images including bone and cartilaginous tissues (Fig. 2 *I*–*M*) from micro-CT scans showed that the olfactory cavity is clearly more structured in WT (Fig. 2*L*) as compared with *Camsap3*$^{tm1a/tm1a}$ (Fig. 2*M*). In neonatal mice, however, we did not observe accumulated mucus in the nasal cavity in either WT or *Camsap3*$^{tm1a/tm1a}$ (*SI Appendix*, Figs. S8 *A* and *B* and S10 *A* and *B*), suggesting that *Camsap3*$^{tm1a/tm1a}$ mice were not born with mucin hyperproduction. Accumulated mucin likely results in the structural abnormality as well as coughing and sneezing symptoms (*SI Appendix*, Fig. S4 and Audio S1) observed in *Camsap3*$^{tm1a/tm1a}$ mice. In addition, the nasal cavity of *Camsap3*$^{tm1a/tm1a}$ exhibited signs of inflammation, as accumulated mucin was populated by leukocytes (*SI Appendix*, Fig. S7 *B* and *C*), suggesting chronic rhinosinusitis.

6) Olfactory sensory neuron (OSN) degeneration. Since progressive loss of olfaction in *Camsap3*$^{tm1a/tm1a}$ mice could also relate to neural defects, we examined OSNs in neonatal and young and older adult animals ($n = 3$ each for WT and *Camsap3*$^{tm1a/tm1a}$). OSNs were stained using the anti-olfactory marker protein antibody. WT mice showed a pseudostratified olfactory epithelium of normal thickness, with mature OSNs and axon bundles at all ages (*SI Appendix*, Fig. S8 *A*, *C*, *E*, and *G*). However, extensive thinning of the olfactory epithelium and fewer mature OSNs were present in *Camsap3*$^{tm1a/tm1a}$ at P1 and 67 with complete loss of OSNs at P204 (*SI Appendix*, Fig. S8 *B*, *D*, *F*, and *H*). The progressive loss of OSNs is consistent with impaired olfaction observed in the behavioral testing of *Camsap3*$^{tm1a/tm1a}$ (Fig. 1*G*). Mucus blockage (labeled "b") is evident in both young and older adult *Camsap3*$^{tm1a/tm1a}$ mice (*SI Appendix*, Fig. S8 *F* and *H*), but not in neonates.

Knockdown of CAMSAP3 Results in Abnormal Cilia on MCCs and Impaired Mucociliary Transport. The several PCD-like phenotypes observed in *Camsap3*$^{tm1a/tm1a}$ prompted us to hypothesize that CAMSAP3 plays important roles in motile cilia. Therefore, we examined the nasal respiratory tract of *Camsap3*^{tm1a} mice in more detail. Samples from the nasal cavity of *Camsap3*$^{tm1a/tm1a}$ and WT ($n = 4$ each) mice at P3 and 20 were examined using scanning electron microscopy (SEM). Cilia of MCCs from *Camsap3*$^{tm1a/tm1a}$ (Fig. 3 *B* and *D* and *SI Appendix*, Fig. S9 *C* and *D*)

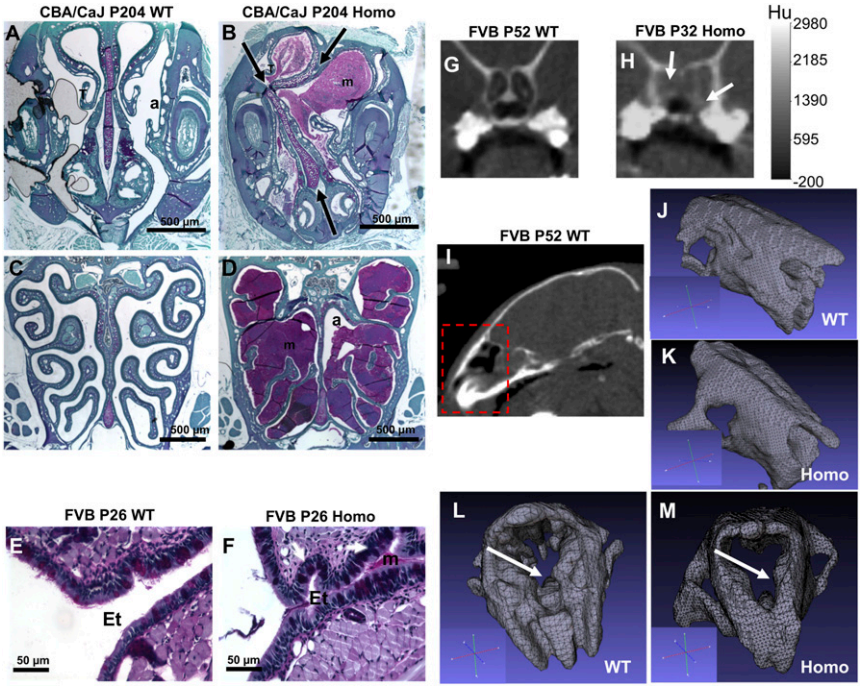

Fig. 2. *Camsap3*$^{tm1a/tm1a}$ mice have obstructed nasal cavities and abnormal nasal cavity structure. (*A–D*) Mucin blocks the nasal airway and obstructs the olfactory epithelium in older *Camsap3*$^{tm1a/tm1a}$ mice. PAS staining for glycoproteins in coronal nasal sections in WT (*A*) showing a patent anterior nasal airway (*A*) with a central bony septum at the level of the vomeronasal organ compared with mucin buildup (*B*) (purple) in *Camsap3*$^{tm1a/tm1a}$ with a deviated septum (arrows). WT (*C*) patent nasal airway with a central septum at a level where the ethmoid turbinates (T) are covered primarily with olfactory sensory epithelium compared with *Camsap3*$^{tm1a/tm1a}$ (*D*) with almost total airway (a) blockage with mucin (purple). (Scale bars, 500 µm.) (*E–H*) Mucin blocks the nasal airway of young adult *Camsap3*$^{tm1a/tm1a}$ mice. PAS staining shows a normal opening to the Eustachian tube (Et) in WT mouse (*E*), while its *Camsap3*$^{tm1a/tm1a}$ littermate exhibited mucin accumulation (m) and folding of epithelial cell layers (white arrows) in the Eustachian tube (*F*). (Scale bars, 50 µm.) Micro-CT images showing dark and radiopaque regions at the back of the nasal cavity in WT (*G*) and *Camsap3*$^{tm1a/tm1a}$ (*H*), respectively. White arrows indicate blockage. A calibration bar is as indicated. Hu, Hounsfield units. (*I–M*) Representative rendered 3D images obtained by thresholding of CT data in WT and *Camsap3*$^{tm1a/tm1a}$ are shown. Snout details from the region outlined in red in *I* are shown for different orientations for WT (*J* and *L*) and *Camsap3*$^{tm1a/tm1a}$ (*K* and *M*) mice. An orientation axis for each figure is shown in the corresponding inset. The white arrows in (*L*) and (*M*) point at the snout region with most structural differences between the WT and *Camsap3*$^{tm1a/tm1a}$mouse.

were in general shorter compared with WT littermates (Fig. 3 *A* and *C* and *SI Appendix*, Fig. S9 *A* and *B*) and were heterogeneous in length and shape. Some cilia were curved and much longer than other cilia on the same cell (Fig. 3*B* and *SI Appendix*, Fig. S9*D*, arrows). In contrast, cilia from WT were straight and of comparable lengths (Fig. 3 *A* and *C* and *SI Appendix*, Fig. S9 *A* and *B*). At P20, the apical surfaces of MCCs in *Camsap3*$^{tm1a/tm1a}$ mice were often covered with a layer of fibrous threads (Fig. 3*E*, arrows and *SI Appendix*, Fig. S9*C*), likely to be mucin-based structures (30, 31). These fibrous threads were seldom found in cilia of P3 samples, suggesting that mucus accumulation was minimal in the nasal cavity at this age. To test whether MCCs have normal mucociliary transport function, we examined ciliary motility of freshly dissected tissues from similar areas of the nasal cavity, tympanic cavity, and trachea of WT, *Camsap3*$^{tm1a/+}$, and *Camsap3*$^{tm1a/tm1a}$ at ages ranging from neonate to young adult. The isolated tissues were washed several times to remove mucus before recording. Similar to a previous report (32), the average cilia beat frequency (CBF) determined at P3 for both WT and *Camsap3*$^{tm1a/+}$ was ~12 Hz. In Fig. 4*A*, CBFs for motile cilia in nasal tissues at P3 in WT, *Camsap3*$^{tm1a/+}$, and *Camsap3*$^{tm1a/tm1a}$ mice were determined from time-lapse images. Mean ± SD for WT was 12.62 ± 2.03; for *Camsap3*$^{tm1a/+}$, 11.98 ± 2.51; and for *Camsap3*$^{tm1a/tm1a}$, 5.52 ± 0.90. The CBFs in *Camsap3*$^{tm1a/+}$ were not statistically different from WT, but both were significantly greater than in *Camsap3*$^{tm1a/tm1a}$ (one-way ANOVA with Dunnett's multiple-comparison test, $P = 0.0001$). A rhythmic beating with a coordinated motion was observed in MCCs of WTs and *Camsap3*$^{tm1a/+}$, but *Camsap3*$^{tm1a/tm1a}$ showed only patches of cilia with slow movements in the nasal cavity (Movies S2 and S3), tympanic cavity of the middle ear (Movies S4 and S5), and trachea (Movies S6 and S7). As shown

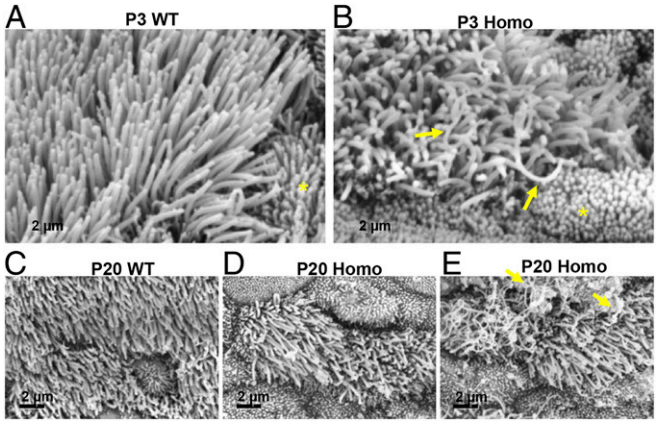

Fig. 3. MCCs from *Camsap3*$^{tm1a/tm1a}$ have abnormal ciliary morphology. SEM images of nasal MCCs from WT (*A* and *C*) and its *Camsap3*$^{tm1a/tm1a}$ littermate (*B*, *D*, and *E*) at P3 and 20. Arrows in *B* point to long and curved cilia in *Camsap3*$^{tm1a/tm1a}$ mice. Nearby microvilli are indicated by asterisks. (*E*) The surface of MCCs from a *Camsap3*$^{tm1a/tm1a}$ at P20. Yellow arrows indicate the layer of fibrous substances. (Scale bars, 2 µm.)

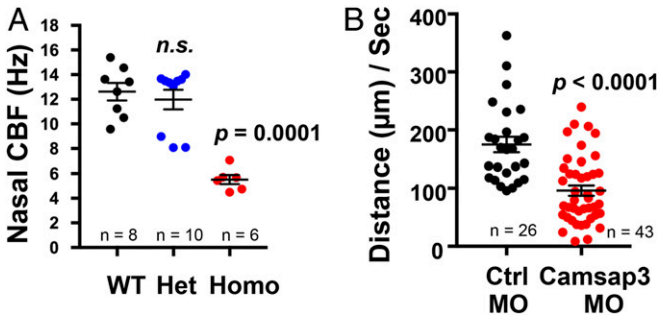

Fig. 4. Reduction of CAMSAP3 causes impaired mucociliary transport. (*A*) Nasal ciliary beat frequency in hertz (beats per second) for motile cilia of nasal tissues at age P3 versus genotype. Replicates (*n*) are as indicated. (*B*) Velocity of fluorescent beads in micrometers per second of control (Ctrl) *Xenopus* embryos injected with morpholinos versus *Camsap3* morpholino-injected embryos. *n*, number of fluorescent beads.

in Movies S2–S7, directional flow of particles across the field of view was observed in WT and *Camsap3*$^{tm1a/+}$ (Movies S2, S4, and S6). Cilia of MCCs from *Camsap3*$^{tm1a/tm1a}$ exhibited non-coordinated beating with various speeds (Movie S3) and sometimes they were motionless (Movies S5 and S7), that is, directional flow was reduced or not observed. The lack of directional flow is an indicator that mucociliary clearance was compromised in *Camsap3*$^{tm1a/tm1a}$ mice.

Because CAMSAP3 is expressed in different tissues and cells, it is possible that reduced clearance observed in MCCs of *Camsap3*$^{tm1a/tm1a}$ is secondary to other defects. For example, increased mucin secretion by potentially dysfunctional submucosal glands and/or goblet cell hyperplasia and mucin accumulation can affect cilia structure and mucociliary clearance. Therefore, we examined goblet cells from neonatal and older adult mice. Goblet cell hyperplasia and excess mucin were not observed in neonatal *Camsap3*$^{tm1a/tm1a}$ when compared with WT mice at P1 using PAS staining for mucus (*SI Appendix*, Figs. S8 *A* and *B* and S10 *A* and *B*). In contrast, defects in ciliary motion and cilia morphology were consistently observed in neonates (Figs. 3*B* and 4*A* and *SI Appendix*, Fig. S9*D*). These data suggest that impaired mucociliary transport was not due to excess mucin at birth. However, accumulated mucin (Fig. 2 *B* and *D*, purple) and goblet cell hyperplasia were observed but only in adult *Camsap3*$^{tm1a/tm1a}$ mice (*SI Appendix*, Fig. S10 *C* and *D*).

To further verify CAMSAP3's role in motile cilia function, morpholino-mediated anti-*Camsap3* oligomers (*Camsap3*-MO) were used to knock down CAMSAP3 expression in MCCs located on the skin of *Xenopus* embryos. Morpholino-mediated random oligomers (control-MOs) were used as negative controls. The mucociliary epithelium of *Xenopus* is similar to mouse, with the important distinction that it occurs on the outer surface of the embryo. Therefore, unlike the constrained internal environment of the mouse, mucosal blockage is not likely to represent a serious issue. Although cilia morphology varied ($n = 7$), that of MCCs with *Camsap3*-MO injection appeared to have fewer and shorter cilia as compared with MCCs with control-MO injection (*SI Appendix*, Fig. S11). To measure cilia-generated flow, fluorescent beads were added onto the surface of *Xenopus* embryos injected with control- or *Camsap3*-MOs and imaged. As shown in Fig. 4*B* and Movies S8 and S9, fluorescent beads on *Camsap3*-MO–injected embryos exhibited statistically slower movement as compared with beads on control-MO–injected embryos. Each dot represents the distance of directional movement for each individual fluorescent bead. Data are collected from 9 control-MO– and 14 *Camsap3*-MO–injected *Xenopus* embryos in two independent experiments. Mean ± SD for control-MO, 174.80 ± 68.39; *Camsap3*-MO, 96.01 ± 57.86; $^{*}P < 0.0001$ (unpaired *t* test). These data further indicate that CAMSAP3 is required for the coordinated motile ciliary movements that underlie mucociliary transportation.

CAMSAP3 Is Located at the Basal Bodies and at the Base of Axonemes of Motile Cilia in Nasal MCCs. To understand the role of CAMSAP3 in motile cilia function, the nasal cavity was examined using anti–CAMSAP3-M. Anti–γ-tubulin (γ-Tub) was used as a basal body marker, while anti–acetylated-α-tubulin (Ac-Tub) was used to label cilia. CAMSAP3 distributions were compared among nasal tissue samples from WT, *Camsap3*$^{tm1a/+}$, and *Camsap3*$^{tm1a/tm1a}$ mice collected at different ages ranging from P3 to 30 (WT, $n = 9$; *Camsap3*$^{tm1a/+}$, $n = 3$; *Camsap3*$^{tm1a/tm1a}$, $n = 9$). CAMSAP3 staining was found at the apical surface of respiratory epithelia, as well as in the acini of submucosal glands that lie within WT mucociliary epithelia (Fig. 5*A* and *SI Appendix*, Fig. S12 *A* and *C*). Lack of staining in *Camsap3*$^{tm1a/tm1a}$ (Fig. 5*B* and *SI Appendix*, Fig. S12*B*) suggests that CAMSAP3 proteins are absent or significantly reduced in the nasal cavity of *Camsap3*$^{tm1a/tm1a}$.

For MCCs in the respiratory epithelia, CAMSAP3 staining (green) showed two distinct lines with similar staining intensity in all WT samples in neonatal mice at P3 (Fig. 5*C*). 1) The upper line of staining is between basal bodies (γ-Tub, red) and axonemes (Ac-Tub, violet). 2) The lower line of staining overlaps with γ-tubulin staining (Fig. 5 *C* and *C′*). For *Camsap3*$^{tm1a/tm1a}$ littermates, some samples did not have CAMSAP3 staining at all, while others had only the lower line (CAMSAP3) that overlapped with γ-tubulin staining, the basal body marker (Fig. 5 *D* and *D′*). As animals became older, most of the MCCs from *Camsap3*$^{tm1a/tm1a}$ did not show CAMSAP3 staining (Fig. 5*F*). However, cells with CAMSAP3 signals were occasionally found aligning with the γ-tubulin staining (lower line) (*SI Appendix*, Fig. S13*B*). This is consistent with the notion that *Camsap3*$^{tm1a/tm1a}$ is a hypomorphic model. In other words, we did not observe the upper line of CAMSAP3 in MCCs from *Camsap3*$^{tm1a/tm1a}$ regardless of age. In contrast, the upper line of CAMSAP3 was present in all WT and *Camsap3*$^{tm1a/+}$ samples. At P30, most WT MCCs had only the upper line, although a few MCCs had double lines with some CAMSAP3 staining located along basal bodies as judged by merged images with γ-tubulin staining (Fig. 5 *E*, *E′*, and *G*). Using structured illumination microscopy (SIM), a separation between green CAMSAP3 dots and red γ-tubulin dots was clearly observed (Fig. 5*G*). The distance between the green CAMSAP3 dots in the upper line and the basal bodies stained with γ-tubulin was measured to be 545 ± 133 nm (mean ± SD; $n = 306$) (Fig. 5*G*). Because CAMSAP3 and CAMSAP2 are similar in structure and function (8, 33), anti–CAMSAP3-M recognizes CAMSAP2 protein, albeit with a lower affinity (*SI Appendix*, Fig. S1*C*). To exclude the possibility that CAMSAP3 signals in MCCs are CAMSAP2, we examined CAMSAP2 expression patterns in MCCs of WT, *Camsap3*$^{tm1a/+}$, and *Camsap3*$^{tm1a/tm1a}$ at P3 and 30 using anti-CAMSAP2. As shown in *SI Appendix*, Fig. S14, MCCs from WT and *Camsap3*$^{tm1a/tm1a}$ have similar CAMSAP2 staining patterns, which are completely different from those of CAMSAP3. In fact, no signals were detected at the axoneme base by anti-CAMSAP2. In summary, CAMSAP3 is expressed between the basal body and the axoneme, where the central MT pair is initiated, as well as at the basal bodies in young animals.

Knockdown of CAMSAP3 Results in Loss of Basal Body Polarity in MCCs. The motile cilium is a complex organelle formed by the axoneme and emanates from the basal body (Fig. 6*A*). Basal bodies have an electron-dense side projection called the basal foot that points in the direction of the effective stroke, as well as a striated rootlet that projects in the opposite direction and is

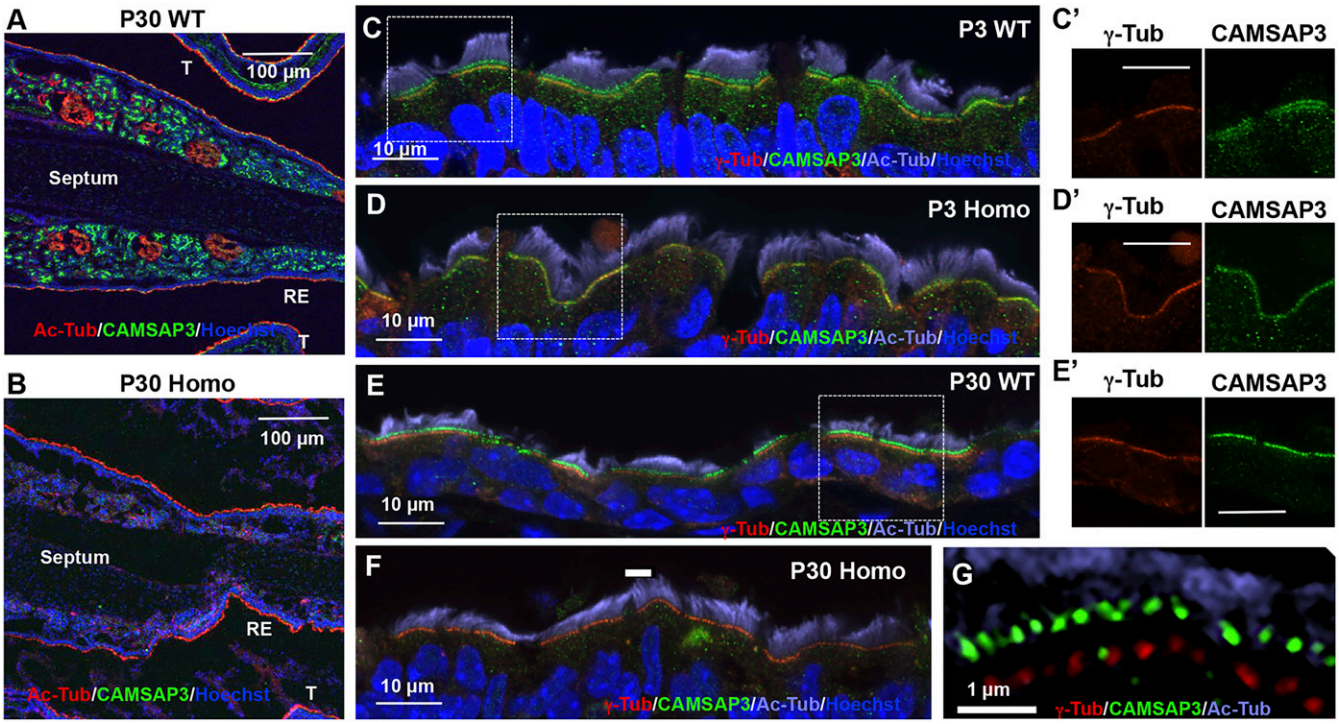

Fig. 5. CAMSAP3 is located at the base of axonemes and at the basal bodies. (*A*–*F*) Immunofluorescent images of nasal MCCs from WT (*A*, *C*, and *E*) and *Camsap3*$^{tm1a/tm1a}$ (*B*, *D*, and *F*) at P3 (*C* and *D*) and 30 (*A*, *B*, and *E*–*G*) are shown. Antibodies include anti–CAMSAP3-M (green), anti–γ-tubulin (red), anti–acetylated-α-tubulin (red in *A* and *B* and violet in *C*–*G*), and Hoechst 33342 (blue, nuclei). Respiratory epithelium (RE). (*G*) SIM image showing the upper CAMSAP3 line (green dots) and lower line of basal bodies (γ-Tub, red dots). (Scale bars, 100 μm [*A* and *B*], 10 μm [*C*–*F*], 5 μm [*C*′, *D*′, and *E*′], and 1 μm [*G*].) *C*′, *D*′, and *E*′ are enlarged images of the boxed regions in *C*–*E* showing anti–γ-tubulin (red) and anti–CAMSAP3-M (green) channels.

thought to anchor the cilium inside the cell. Both the basal foot and the striated rootlet are reliable determinants of cilia polarity (34). In WT tissues including the nasal cavity, basal feet are unidirectional (20, 21). Although PCP signaling instructs MCC polarity, hydrodynamic forces driven by cilia motility are critical for coordinating cilia polarity along the axis of cell polarity (35–37). Additionally, the basal feet and their orientation are critical for the synchronized beating needed for mucociliary transportation (30, 38). Based on the location of CAMSAP3 (Fig. 5), we forecast that lack of CAMSAP3 in MCCs may change the orientation of basal bodies. To test this possibility, the basal feet (position "b" in Fig. 6*A*) in MCCs of WT and *Camsap3*$^{tm1a/tm1a}$ were examined by transmission electron microscopy (TEM). Although the basal feet were not unidirectional in the nasal MCCs of *Camsap3*$^{tm1a/tm1a}$ (Fig. 6 *B* and *C*, yellow arrows), they were nicely aligned in WT (*SI Appendix*, Fig. S15). Since ciliogenesis is well-conserved throughout eukaryotes (26, 39), we further investigated the orientation of cilia in MCCs of *Xenopus* embryos, where polarity has been extensively studied (22). Specifically, control- or *Camsap3*-MOs were injected, together with messenger ribonucleic acids (mRNAs) for RFP-centrin (a basal body marker) and CLAMP-GFP (a striated rootlet marker). We observed a uniform array of cilia in control-MO–injected embryos (Fig. 7 *A* and *A*′), while in *Camsap3*-MO–injected embryos the cilia orientation was disorganized (Fig. 7 *B* and *B*′). The phenotype was quantified by measuring cilia orientation (Fig. 7*C*). In these graphs, the direction of the arrow represents the mean orientation of the cilia within a given cell and is a readout of cell polarity. Additionally, the length of the arrow represents variation around the mean such that a long

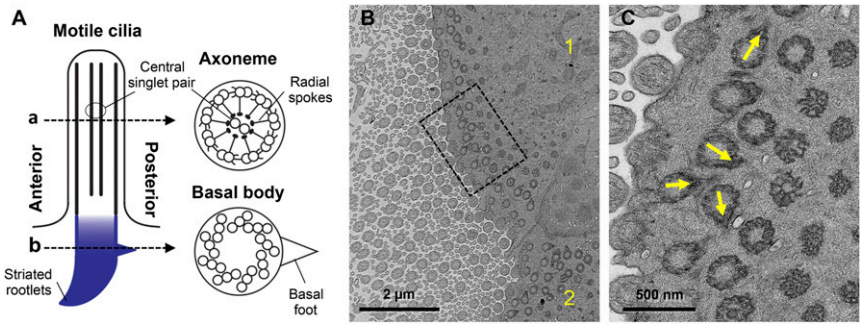

Fig. 6. Reduction of CAMSAP3 expression in mice disrupts the polarity of basal bodies in MCCs. (*A*) Motile cilium structure. (*B*) A representative image showing disorientated basal feet found in two MCCs (indicated with numbers 1 and 2) in the nasal cavity of *Camsap3*$^{tm1a/tm1a}$ (P30). (Scale bar, 2 μm.) (*C*) High-magnification image of the boxed region in *B*. Yellow arrows indicate basal feet with various orientations. (Scale bar, 500 nm.)

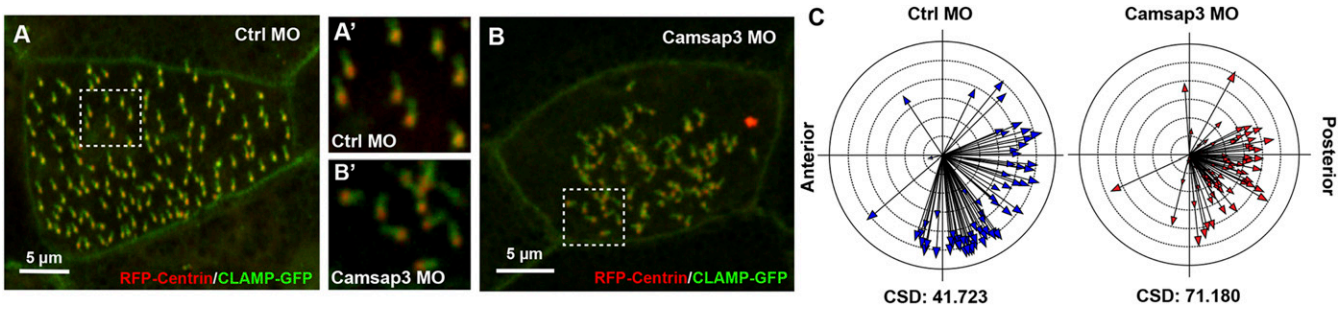

Fig. 7. Reduction of CAMSAP3 expression disrupts the polarity of basal bodies in MCCs of *Xenopus* embryos. Confocal images of *Xenopus* embryos injected with RNAs for RFP-centrin and CLAMP-GFP together with either control- (*A*) or *Camsap3*-MO (*B*). Boxed regions from *A* and *B* are shown in *A′* and *B′*, respectively. (Scale bars, 5 μm.) (*C*) Quantification of MCC polarity. Each arrow represents the mean cilia orientation for a given cell, while arrow length represents 1/*r*, namely the variation in orientation within the cell (long arrows indicate low variation and short arrows indicate high variation).

arrow represents a coordinated cell. Circular SD (CSD) is a metric for cumulative variation and increases from 41.72 in the control-MO to 71.18 in the *Camsap3*-MO in four independent experiments (control-MO embryos, $n = 8$; *Camsap3*-MO embryos, $n = 11$; $P < 0.0001$). Importantly, while the cilia are disorganized in *Camsap3*-MO cells, the mean cilia orientation is still in the posterior direction, indicating that PCP-driven cell polarity is maintained. Taken together, our data suggest that reduced CAMSAP3 expression results in the loss of basal body polarity. Motility defects likely underlie the inability of cilia to refine their orientation, consistent with what has been observed in PCD-related mutations (35).

Central MT Pairs Are Rare in Cilia of MCCs from *Camsap3*$^{tm1a/tm1a}$ Mice. The axoneme of MCCs is composed of the 9 + 2 MT skeleton, while basal bodies have nine triplet MTs and lack a central MT (Fig. 6*A*). Since CAMSAP3 was also located at the base of axonemes (Fig. 5), where the central MT pair is initiated, and CAMSAP3 proteins can act as seeds for MT elongation (8, 10), we examined axoneme structure ("a" position in Fig. 6*A*) in MCCs of WT and *Camsap3*$^{tm1a/tm1a}$ using TEM (Fig. 8). Although both inner and outer dynein arms (red arrows in Fig. 8) were present in the nine MT doublets, we discovered several structural abnormalities in the axonemes of MCCs from *Camsap3*$^{tm1a/tm1a}$ (Fig. 8*B*). The phenotypes were divided into five groups, as shown in Fig. 8*C*: 1) 9 + 0, in which the axoneme has only outer doublets (Fig. 8*A*); 2) 8 + 1, in which the axoneme has eight outer doublets and one doublet MT mislocalized at the center (Fig. 8*B*); 3) 9 + 1, in which the axoneme has nine outer doublets and one inner singlet (Fig. 8*C*); 4) 9 + 2, in which the axoneme has nine outer doublets and two normal MT singlets (Fig. 8*D*); and 5) unclassified (Fig. 8*E*). Among 128 axonemes examined, 64.1% were type 1 (9 + 0); 13.3% were type 2 (8 + 1); 11.7% were type 3 (9 + 1); 5.5% were type 4 (9 + 2); and 5.4% were unclassified. In other words, most of the cilia (89.1%) in *Camsap3*$^{tm1a/tm1a}$ had abnormal central MT pairs or were missing the central pair entirely, suggesting that CAMSAP3 is needed for central MT-pair formation.

Discussion

The results of this study are summarized as follows. 1) CAMSAP3-KD mice exhibit some PCD-like phenotypes. 2) Knocking down CAMSAP3 protein levels produces structural and functional defects in motile cilia of MCCs in both mice and frogs. 3) CAMSAP3

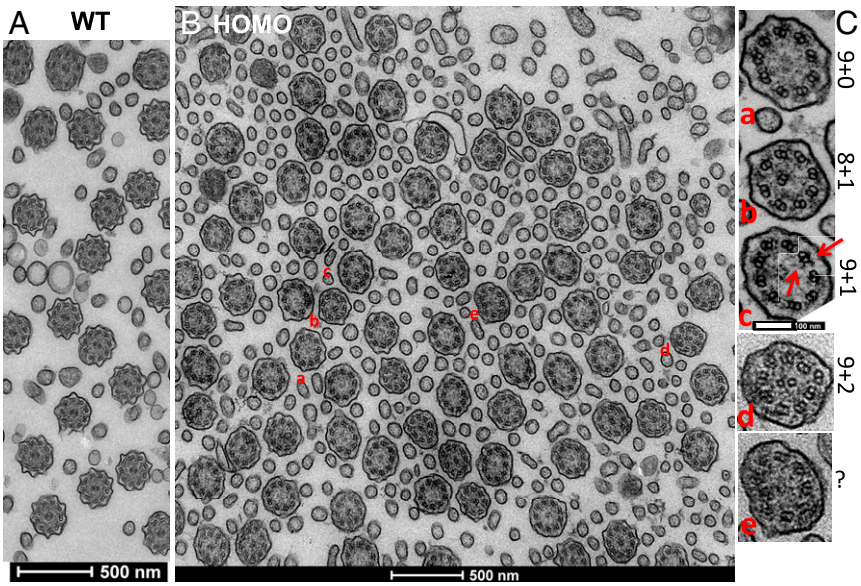

Fig. 8. CAMSAP3 is needed for the formation of central MT pairs in axonemes. TEM images showing MT arrays in axonemes from an adult P30 WT (*A*) compared with a P30 *Camsap3*$^{tm1a/tm1a}$ (*B*). Five different axoneme MT configurations (*a*–*e*) are listed in *C*. Red arrows point to inner and outer dynein arms in outer MT doublets. (Scale bars, 500 nm [*A* and *B*] and 100 nm [*C*].)

is expressed along the basal bodies and at the base of axonemes in MCCs. 4) MCCs in CAMSAP3-KD mice show disorientated basal bodies and lack the central MT pair in the axoneme. Collectively, our data suggest that CAMSAP3 plays an important role in forming central MT pairs, orienting the basal bodies in MCCs, and facilitating cilia motility.

Our study of *Camsap3*-KD mice on three different backgrounds revealed that CAMSAP3-related phenotypes were strain-dependent. The C57BL/6 (B6) strain appears more vulnerable to ciliary defects as previously reported in transgenic models for PCD (40). In fact, mRNA expression profiles for PCD models on B6 and other strains are significantly different in several gene clusters, including genes involved in cilia formation and function (41). Hence, further investigation is needed to understand how genetic modifications relate to specific PCD-like phenotypes.

CAMSAP3 is widely expressed in different tissues and cell types. Therefore, the phenotypes reported in this study may relate to several deficiencies that occur in multiple cells/tissues in addition to motile cilia defects. For example, preweaning mortality was suggested to be caused by a defect in the placenta (11). An abnormal placenta may also contribute to the lower litter size that was only observed in $Camsap3^{tm1a/tm1a}$ females in addition to dysfunctional motile cilia located in the reproductive tract (Fig. 1*F*). Although accumulated mucus or change in airflow in the nasal cavity often results in unusual nasal structures (42) that are also found in other PCD mice (43), CAMSAP3 may have other functions that contribute to craniofacial abnormalities, requiring systematic investigation in $Camsap3^{tm1a}$ mice.

The central MT pair is critical for MCCs to generate the coordinated planar motion required for mucus clearance (23, 24). One of the long-standing questions in ciliogenesis is how the central MT pair is assembled and what components are involved. We found that the MT-minus end regulator CAMSAP3 localizes to where the central pair initiates, suggesting a role in central-pair formation. Analysis of patients with PCD has identified a subset of structural defects associated with the disease. In particular, patients have been identified with mutations in hydin, Rsph4A, and Rsph9, all of which lead to central-pair defects (44–47). In this report, we identify CAMSAP3 as an additional potential candidate to be included in this class of mutations. Intriguingly, the central MT pairs extend from a region near the transition zone, which is ~500 nm in length (23, 48, 49). It is of interest, therefore, that CAMSAP3 is located more than 500 nm away from the center of the basal bodies, that is, at the distal end of the transition zone. CAMSAP3 is also known to interact with the MT-severing protein katanin, mutations of which have been shown to cause central-pair defects in *Tetrahymena* (6, 50, 51). It is, therefore, tempting to speculate that the balance between the nucleation regulated by CAMSAP3 and the destruction regulated by katanin represents a critical nexus for the control of central-pair formation.

MT networks in individual cells are organized to perform different cellular functions. For neurons, CAMSAP3 sustains nonacetylated MTs in order to maintain neuronal polarity (12). For epithelial cells, CAMSAP3 is reported to regulate the polarity of MTs and influence the distribution of organelles, such as Golgi and nuclei, as reported in *Camsap3*-knockout (KO) and *Camsap3*-knockin ($Camsap3^{dc/dc}$) mouse models, as well as in several cell lines (1, 13, 14, 52). However, mispositioning of organelles was not obvious in MCCs of $Camsap3^{tm1a/tm1a}$ (Fig. 5) because the basal bodies were all located under the axoneme at the apical cortex, and nuclei appeared on the basal sides of MCCs. One possibility for the lack of abnormal organelle distribution in MCCs of $Camsap3^{tm1a/tm1a}$ is that CAMSAP2 could compensate for some functions of CAMSAP3 to maintain the MT networks of MCCs as previously reported in other cells (33). Indeed, we found similar staining patterns in $Camsap3^{tm1a/tm1a}$ and their WT littermates (*SI Appendix*, Fig. S14), showing that CAMSAP2 is expressed throughout the cytoplasm in neonates and colocalizes with the basal bodies at the apical cortex in adults. Further investigation is needed to understand the roles of CAMSAP2 and CAMSAP3 for establishing and maintaining differentiated MCCs.

Dense MT networks at the apical cortex of MCCs control basal body positioning and are essential for synchronizing motile ciliary movements (30, 38, 53). However, it is not fully known how the MT networks are formed around basal bodies. In addition to localizing to the base of the axoneme, we found that CAMSAP3 is present in neonates along the basal bodies (Fig. 5 *C* and *C′*), suggesting that CAMSAP3 could play an important role in establishing MT networks at the apical cortex. It is known that apical and subapical actin networks are also important for establishing ciliary spacing and polarity, as well as for coordinating metachronal synchrony (22, 38, 54). Since CAMSAP3 can influence apical actin networks through its interaction with ACF7 (5, 55), we suspect that CAMSAP3 may facilitate the establishment and coordination of cytoskeletal networks in the apical cortex through its interaction with both MTs and actin filaments. Understanding how CAMSAP3 facilitates the establishment and coordination of cytoskeletal networks requires further study.

Motile cilia are only present in specific tissues and cell types. In contrast, most cells in our body have primary cilia that are sensory organelles. A majority of primary cilia have MTs in the 9 + 0 configuration, that is, they do not have a central MT pair. As shown in *SI Appendix*, Fig. S16, CAMSAP3 signals do not colocalize with the basal bodies of primary cilia. In addition, the reduction of CAMSAP3 in $Camsap3^{tm1a/tm1a}$ shows that the location and morphology of basal bodies in primary cilia on cochlear epithelial cells are similar to those of WT. This observation is consistent with previous reports showing that CAMSAP3 is not centrosome-bound. In fact, CAMSAP3 is often found along noncentrosomal MTs or in pericentrosomal areas, where it is involved in releasing MTs from the centrosome (4, 8, 51, 56). We also acknowledge that a minority of primary cilia, like OSNs, can display the 9 + 2 configuration. At present, it is not known whether OSNs in $Camsap3^{tm1a/tm1a}$ mice retain normal 9 + 2 cilia, but these animals were born with fewer OSNs (*SI Appendix*, Fig. S8 *A–D*). Although OSN loss in older adult $Camsap3^{tm1a/tm1a}$ mice (*SI Appendix*, Fig. S8*H*) could be a consequence of mucus obstruction (Fig. 2) and/or inflammatory changes (*SI Appendix*, Fig. S7) due to dysfunctional MCCs of $Camsap3^{tm1a/tm1a}$, the abnormality of OSNs observed in neonates is clearly unrelated to motile cilia dysfunction of MCCs. In addition, CAMSAP3 might serve to maintain OSN polarity by regulating MT stability, as observed in hippocampal neurons (12). In other words, OSN loss observed in $Camsap3^{tm1a/tm1a}$ mice is likely a combination of defects in several different kinds of cells. To determine how lack of CAMSAP3 in OSNs contributes to their loss in $Camsap3^{tm1a/tm1a}$ will require a specific conditional KO model.

In conclusion, CAMSAP3 is involved in many physiological functions through its associated protein partners, suggesting that this minus-end MT regulator may influence ciliogenesis and cilia function via several different mechanisms, including microtubule organization, material trafficking, organelle positioning, and so forth. Hence, divergent phenotypes are to be expected when conditional knockout mouse models become available to investigate CAMSAP3's role in specific cells and tissues. Nevertheless, the data obtained from this study identify CAMSAP3 as a critical component of motile cilia, providing scientific knowledge that is fundamental to the basic biology regarding cilia function.

Materials and Methods

Camsap3^{tm1a} mice are described in *SI Appendix*. The full procedures for evaluation of olfaction, measurements of ciliary motion and ciliary orientation, sound recording and analysis, histochemistry, TEM, SEM, micro-CT and MRI, IF, RT-PCR, Western blot, cell culture, and transfection are provided in *SI Appendix*, where the statistical analyses are also described.

Data and Materials Availability. Data generated or analyzed during this study are included in this article and its supplementary files. All data, including the original images from micro-CT and MRI, will be made available upon request to the corresponding author.

ACKNOWLEDGMENTS. We thank Drs. Jonathan Siegel, Donna Whitlon (Northwestern University), and Masatoshi Takeichi (RIKEN Center for Developmental Biology) for providing instruments and reagents, and Mr. Taewoo Kim (Northwestern University) for participating in the data analysis. Imaging work was performed at the Northwestern University Center for Advanced Microscopy, which is supported by National Cancer Institute (NCI) grant CCSG P30 CA060553 and National Institutes of Health NIH grant 1S10OD016342-01. MRI and CT scans were conducted at the Center for Translational Imaging Small Animal Imaging Laboratory. Rederivation of *Camsap3*^{tm1a} lines was performed by the Transgenic and Targeted Mutagenesis Laboratory of Northwestern University. This research was funded by the Knowles Hearing Center (to J.Z.) and by National Institute on Deafness and Other Communication Disorders (NIDCD) grant R56 DC011813 (to J.Z.), grant DC000089 (to M.A.C.), and grant GM089970 (to B.J.M.).

1. J. Zheng *et al*., Marshalin, a microtubule minus-end binding protein, regulates cytoskeletal structure in the organ of Corti. *Biol. Open* **2**, 1192–1202 (2013).
2. S. S. Goodwin, R. D. Vale, Patronin regulates the microtubule network by protecting microtubule minus ends. *Cell* **143**, 263–274 (2010).
3. M. C. Hendershott, R. D. Vale, Regulation of microtubule minus-end dynamics by CAMSAPs and Patronin. *Proc. Natl. Acad. Sci. U.S.A.* **111**, 5860–5865 (2014).
4. W. Meng, Y. Mushika, T. Ichii, M. Takeichi, Anchorage of microtubule minus ends to adherens junctions regulates epithelial cell-cell contacts. *Cell* **135**, 948–959 (2008).
5. W. Ning *et al*., The CAMSAP3-ACF7 complex couples noncentrosomal microtubules with actin filaments to coordinate their dynamics. *Dev. Cell* **39**, 61–74 (2016).
6. K. Jiang *et al*., Structural basis of formation of the microtubule minus-end-regulating CAMSAP-katanin complex. *Structure* **26**, 375–382.e4 (2018).
7. S. Takahashi *et al*., Cadherin 23-C regulates microtubule networks by modifying CAMSAP3's function. *Sci. Rep.* **6**, 28706 (2016).
8. K. Jiang *et al*., Microtubule minus-end stabilization by polymerization-driven CAMSAP deposition. *Dev. Cell* **28**, 295–309 (2014).
9. D. Nashchekin, A. R. Fernandes, D. St Johnston, Patronin/shot cortical foci assemble the noncentrosomal microtubule array that specifies the *Drosophila* anterior-posterior axis. *Dev. Cell* **38**, 61–72 (2016).
10. J. Zenker *et al*., A microtubule-organizing center directing intracellular transport in the early mouse embryo. *Science* **357**, 925–928 (2017).
11. V. Perez-Garcia *et al*., Placentation defects are highly prevalent in embryonic lethal mouse mutants. *Nature* **555**, 463–468 (2018).
12. V. Pongrakhananon *et al*., CAMSAP3 maintains neuronal polarity through regulation of microtubule stability. *Proc. Natl. Acad. Sci. U.S.A.* **115**, 9750–9755 (2018).
13. M. Toya *et al*., CAMSAP3 orients the apical-to-basal polarity of microtubule arrays in epithelial cells. *Proc. Natl. Acad. Sci. U.S.A.* **113**, 332–337 (2016).
14. A. Muroyama, M. Terwilliger, B. Dong, H. Suh, T. Lechler, Genetically induced microtubule disruption in the mouse intestine impairs intracellular organization and transport. *Mol. Biol. Cell* **29**, 1533–1541 (2018).
15. N. Spassky, A. Meunier, The development and functions of multiciliated epithelia. *Nat. Rev. Mol. Cell Biol.* **18**, 423–436 (2017).
16. E. R. Brooks, J. B. Wallingford, Multiciliated cells. *Curr. Biol.* **24**, R973–R982 (2014).
17. J. L. Stubbs, E. K. Vladar, J. D. Axelrod, C. Kintner, Multicilin promotes centriole assembly and ciliogenesis during multiciliate cell differentiation. *Nat. Cell Biol.* **14**, 140–147 (2012).
18. S. P. Choksi, G. Lauter, P. Swoboda, S. Roy, Switching on cilia: Transcriptional networks regulating ciliogenesis. *Development* **141**, 1427–1441 (2014).
19. C. Boutin *et al*., A dual role for planar cell polarity genes in ciliated cells. *Proc. Natl. Acad. Sci. U.S.A.* **111**, E3129–E3138 (2014).
20. R. De Iongh, J. Rutland, Orientation of respiratory tract cilia in patients with primary ciliary dyskinesia, bronchiectasis, and in normal subjects. *J. Clin. Pathol.* **42**, 613–619 (1989).
21. E. Herawati *et al*., Multiciliated cell basal bodies align in stereotypical patterns coordinated by the apical cytoskeleton. *J. Cell Biol.* **214**, 571–586 (2016).
22. M. E. Werner, B. J. Mitchell, Understanding ciliated epithelia: The power of *Xenopus*. *Genesis* **50**, 176–185 (2012).
23. T. D. Loreng, E. F. Smith, The central apparatus of cilia and eukaryotic flagella. *Cold Spring Harb. Perspect. Biol.* **9**, a028118 (2017).
24. J. Zheng *et al*., Microtubule-bundling protein Spef1 enables mammalian ciliary central apparatus formation. *J. Mol. Cell Biol.* **11**, 67–77 (2019).
25. K.-F. Lechtreck, T. J. Gould, G. B. Witman, Flagellar central pair assembly in *Chlamydomonas reinhardtii*. *Cilia* **2**, 15 (2013).
26. D. R. Mitchell, Speculations on the evolution of 9+2 organelles and the role of central pair microtubules. *Biol. Cell* **96**, 691–696 (2004).
27. W. C. Skarnes *et al*., A conditional knockout resource for the genome-wide study of mouse gene function. *Nature* **474**, 337–342 (2011).
28. G. Testa *et al*., A reliable lacZ expression reporter cassette for multipurpose, knockout-first alleles. *Genesis* **38**, 151–158 (2004).
29. J. K. White *et al*.; Sanger Institute Mouse Genetics Project, Genome-wide generation and systematic phenotyping of knockout mice reveals new roles for many genes. *Cell* **154**, 452–464 (2013).
30. D. K. Clare *et al*., Basal foot MTOC organizes pillar MTs required for coordination of beating cilia. *Nat. Commun.* **5**, 4888 (2014).
31. L. S. Ostedgaard *et al*., Gel-forming mucins form distinct morphologic structures in airways. *Proc. Natl. Acad. Sci. U.S.A.* **114**, 6842–6847 (2017).
32. M. A. Chilvers, C. O'Callaghan, Analysis of ciliary beat pattern and beat frequency using digital high speed imaging: Comparison with the photomultiplier and photodiode methods. *Thorax* **55**, 314–317 (2000).
33. N. Tanaka, W. Meng, S. Nagae, M. Takeichi, Nezha/CAMSAP3 and CAMSAP2 cooperate in epithelial-specific organization of noncentrosomal microtubules. *Proc. Natl. Acad. Sci. U.S.A.* **109**, 20029–20034 (2012).
34. T. J. Park, B. J. Mitchell, P. B. Abitua, C. Kintner, J. B. Wallingford, Dishevelled controls apical docking and planar polarization of basal bodies in ciliated epithelial cells. *Nat. Genet.* **40**, 871–879 (2008).
35. D. R. Mitchell, The evolution of eukaryotic cilia and flagella as motile and sensory organelles. *Adv. Exp. Med. Biol.* **607**, 130–140 (2007).
36. B. Mitchell *et al*., The PCP pathway instructs the planar orientation of ciliated cells in the *Xenopus* larval skin. *Curr. Biol.* **19**, 924–929 (2009).
37. B. Guirao *et al*., Coupling between hydrodynamic forces and planar cell polarity orients mammalian motile cilia. *Nat. Cell Biol.* **12**, 341–350 (2010).
38. K. Kunimoto *et al*., Coordinated ciliary beating requires Odf2-mediated polarization of basal bodies via basal feet. *Cell* **148**, 189–200 (2012).
39. S. Zhang, B. J. Mitchell, Basal bodies in *Xenopus*. *Cilia* **5**, 2 (2016).
40. R. Finn, C. C. Evans, L. Lee, Strain-dependent brain defects in mouse models of primary ciliary dyskinesia with mutations in Pcdp1 and Spef2. *Neuroscience* **277**, 552–567 (2014).
41. C. W. McKenzie *et al*., Strain-specific differences in brain gene expression in a hydrocephalic mouse model with motile cilia dysfunction. *Sci. Rep.* **8**, 13370 (2018).
42. D. M. Coppola, B. A. Craven, J. Seeger, E. Weiler, The effects of naris occlusion on mouse nasal turbinate development. *J. Exp. Biol.* **217**, 2044–2052 (2014).
43. I. Ibañez-Tallon, S. Gorokhova, N. Heintz, Loss of function of axonemal dynein Mdnah5 causes primary ciliary dyskinesia and hydrocephalus. *Hum. Mol. Genet.* **11**, 715–721 (2002).
44. L. Jeanson *et al*., RSPH3 mutations cause primary ciliary dyskinesia with central-complex defects and a near absence of radial spokes. *Am. J. Hum. Genet.* **97**, 153–162 (2015).
45. V. H. Castleman *et al*., Mutations in radial spoke head protein genes RSPH9 and RSPH4A cause primary ciliary dyskinesia with central-microtubular-pair abnormalities. *Am. J. Hum. Genet.* **84**, 197–209 (2009).
46. K.-F. Lechtreck, T. J. Gould, G. B. Witman, Flagellar central pair assembly in *Chlamydomonas reinhardtii*. *Cilia* **2**, 15 (2013).
47. H. R. Dawe, M. K. Shaw, H. Farr, K. Gull, The hydrocephalus inducing gene product, Hydin, positions axonemal central pair microtubules. *BMC Biol.* **5**, 33 (2007).
48. S. Dean, F. Moreira-Leite, V. Varga, K. Gull, Cilium transition zone proteome reveals compartmentalization and differential dynamics of ciliopathy complexes. *Proc. Natl. Acad. Sci. U.S.A.* **113**, E5135–E5143 (2016).
49. T. T. Yang *et al*., Superresolution pattern recognition reveals the architectural map of the ciliary transition zone. *Sci. Rep.* **5**, 14096 (2015).
50. N. Sharma *et al*., Katanin regulates dynamics of microtubules and biogenesis of motile cilia. *J. Cell Biol.* **178**, 1065–1079 (2007).
51. C. Dong *et al*., CAMSAP3 accumulates in the pericentrosomal area and accompanies microtubule release from the centrosome via katanin. *J. Cell Sci.* **130**, 1709–1715 (2017).
52. J. Wang *et al*., CAMSAP3-dependent microtubule dynamics regulates Golgi assembly in epithelial cells. *J. Genet. Genomics* **44**, 39–49 (2017).
53. M. E. Werner *et al*., Actin and microtubules drive differential aspects of planar cell polarity in multiciliated cells. *J. Cell Biol.* **195**, 19–26 (2011).
54. K. Tateishi, T. Nishida, K. Inoue, S. Tsukita, Three-dimensional organization of layered apical cytoskeletal networks associated with mouse airway tissue development. *Sci. Rep.* **7**, 43783 (2017).
55. I. Noordstra *et al*., Control of apico-basal epithelial polarity by the microtubule minus-end-binding protein CAMSAP3 and spectraplakin ACF7. *J. Cell Sci.* **129**, 4278–4288 (2016).
56. A. N. Rao *et al*., Sliding of centrosome-unattached microtubules defines key features of neuronal phenotype. *J. Cell Biol.* **213**, 329–341 (2016).